Elastic and inelastic low-energy electron scattering from pyridine

(ID) **He Su,** (ID) **Xinlu Cheng,** (ID) **Bridgette Cooper, et al.**

View Online   Export Citation   CrossMark

ARTICLES YOU MAY BE INTERESTED IN

Excitation and fragmentation of the dielectric gas C_4F_7N: Electrons vs photons
The Journal of Chemical Physics **158**, 014303 (2023); https://doi.org/10.1063/5.0130216

Elastic and inelastic cross sections for low-energy electron collisions with pyrimidine
The Journal of Chemical Physics **136**, 144310 (2012); https://doi.org/10.1063/1.3702629

Cross Sections for Electron Collisions with NO, N_2O, and NO_2
Journal of Physical and Chemical Reference Data **48**, 043104 (2019); https://doi.org/10.1063/1.5114722

AIP Publishing

Elastic and inelastic low-energy electron scattering from pyridine

View Online   Export Citation   CrossMark

He Su,[1,2]   Xinlu Cheng,[3]   Bridgette Cooper,[2]   Jonathan Tennyson,[2,a]   and Hong Zhang[1,a]

AFFILIATIONS

[1] College of Physics, Sichuan University, Chengdu 610065, China
[2] Department of Physics and Astronomy, University College London, London WC1E 6BT, United Kingdom
[3] Institute of Atomic and Molecular Physics, Sichuan University, Chengdu 610065, China

[a] Authors to whom correspondence should be addressed: j.tennyson@ucl.ac.uk and hongzhang@scu.edu.cn

ABSTRACT

A comprehensive investigation of elastic and inelastic electron scattering from molecular pyridine is reported using the *ab initio* R-matrix method with the static exchange plus polarization and close-coupling approximations for incident energies up to 10 eV. The two well-known low-lying $1\,^2B_1$ and $1\,^2A_2$ shape resonances as well as a $2\,^2B_1$ mixed-character resonance compare well with the theoretical and experimental results. We also detect five core-excited resonances ($1\,^2A_1$, $1\,^2B_2$, $3\,^2B_1$, $2\,^2A_2$, and $4\,^2B_1$), which lie above the first electronic excitation threshold. The total elastic cross sections and momentum transfer cross sections agree reasonably with previous reference data. Comparisons of the differential elastic cross sections of pyridine with those measured for benzene, pyrazine, and pyrimidine show remarkable agreement at scattering angles above $40°$ but behave differently for forward scattering below $40°$ below 6 eV, due to the dominant effect of the permanent dipole moment on the differential cross section in the low energy region with narrow scattering angles. Inelastic electronic excitation cross sections are presented, showing the influence of core-excited resonances below the ionization threshold for the first time.

Published under an exclusive license by AIP Publishing. https://doi.org/10.1063/5.0127540

I. INTRODUCTION

Understanding and characterizing electron scattering from large molecules provides quantitative information and detailed insight into biomolecular systems, particularly in the field of radiation-induced damage to DNA and its constituents.[1,2] Pyridine, with the chemical formula C_5H_5N, is an important N-heterocyclic compound obtained by replacing a CH group in benzene by a nitrogen atom, as shown in Fig. 1. It is used as a solvent[3] and in the preparation of other applications such as drugs, B-group vitamins, colors, rubber products, etc.[4,5] In a seminal study, Boudaïffa *et al.*[6] identified that resonances resulting from low-energy electron collisions are partly responsible for DNA strand breaks in biological systems; see also Huels *et al.*[7] This study has stimulated a huge amount of work characterizing low-energy resonances in small organic molecules.[1,8–12] These studies have largely concentrated shape resonances lying below the first electronic excitation threshold of the given molecule; however, Boudaïffa *et al.* identified resonances in the 6–8 eV region, which is usually above this electronic excitation threshold, as playing a key role in the process.

A literature survey reveals only a few studies on electron-impact scattering by pyridine. For electron scattering, the complete energy regime can be divided into two parts, below the ionization threshold energy (around 10 eV for pyridine) and the intermediate to high energy regions. Low-energy electron scattering phenomena involve energy transfer processes, which are found to occur most effectively through resonances. Earlier measurements mainly identified low-lying resonances. For example, Nenner and Schulz[13] as well as Modelli and Burrow[14] investigate experimentally temporary negative ion formation in electron interactions with pyridine and its substituents. They characterize three low-lying (below 5 eV) π^* resonances in all these targets. Nenner and Schulz[13] suspected that the third resonance was a shape resonance mixed with a core-excited resonance associated with low-lying excited states of the molecule. Mathur and Hasted[15] reported resonant states in the energy range from 0.05 to 10 eV using electron transmission spectrum measurements. Lately, Ryszka *et al.*[16] also presented high resonances with positions no more than 10 eV by analysis of dissociative electron attachment results. The total cross sections for electron impact on pyridine were measured by Dubuis *et al.*[17] between 10
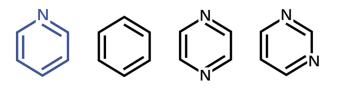
FIG. 1. Molecular structure of pyridine, benzene, pyrazine, and pyrimidine, respectively.

and 1000 eV, Lozano et al.[18] in the energy range 1–200 eV, and Szmytkowski et al.[19] from 0.6 to 300 eV. There are few theoretical studies of electron scattering from pyridine, especially ones that consider inelastic scattering processes. Gholami et al.[20] reported electron impact total cross section, total elastic, total inelastic, and differential cross sections for pyridine using the independent atom mode screening-corrected additivity rule (IAM-SCAR) method over an incident energy range of 10–30 000 eV. In the low energy range, elastic electron scattering from pyridine was studied computationally using the Schwinger multichannel (SMC) method[21] for energies ranging from 0.1 to 12 eV. The authors reported elastic cross sections as well as the positions of the three lowest-lying π^* resonances. Sieradzka et al.[22] give elastic cross sections in the energy range 1–1000 eV using the R-matrix and the IAM-SCAR methods, and subsequently Sieradzka[23] gave a more comprehensive analysis of integral and differential elastic cross sections as well as resonances by using the same method. More recently, Costa et al.[24] gives a summary of electron scattering cross sections for pyridine in the energies 0.1–100 eV, based on their measurements and calculations. The comparison of electron scattering from pyridine with benzene and diazines, see Fig. 1, allows us to investigate how the single or double substitution of the methine group in the benzene ring influences the scattering processes, especially for the effect of the dipole moment on the electron scattering dynamics. Benzene and pyrazine have no permanent dipole moment, while the polar pyridine and pyrimidine molecules have comparable large measured dipole moments, 2.19[25] and 2.334 D,[26] respectively. Elastic and inelastic electron collisions with benzene,[27,28] pyrimidine,[29–31] and pyrazine[31–34] have been studied by several groups.

The present work employs the *ab initio* R-matrix method to identify higher-lying resonances not reported before for electrons scattering on pyridine and give a comprehensive analysis of elastic and inelastic cross sections for incident energy up to 10 eV. This paper is organized as follows: in Sec. II, we introduce the R-matrix methodology, Sec. III presents the target and scattering models, Sec. IV is devoted to results and discussions and finally, we end up with conclusions of the present work in Sec. V.

II. R-MATRIX THEORY

The R-matrix methodology has been extensively applied to the study of electron–molecule scattering calculations at low energies and has been thoroughly reviewed by Tennyson[35] and Burke.[36] We therefore only give the points associated with electrons scattering on pyridine in the present work. The configuration space for electron molecule scattering can be divided into inner and outer regions by a sphere of radius a, centered on the pyridine center-of-mass. In the inner region, the scattering electron is indistinguishable from the target electrons, and therefore both correlation and exchange effects

need to be considered. In the outer region, the exchange effects can be neglected, and only the effect of long-range potential is considered. Within the inner region, the wavefunction of target plus scattering electron ($N + 1$) system can be represented by

$$\Psi_k^{N+1}(x_1, \ldots, x_{N+1}) = A \sum_{ij} a_{ijk} \varphi_i^N(x_1, \ldots, x_N) u_{ij}(x_{N+1}) + \sum_i b_{ik} \chi_i^{N+1}(x_1, \ldots, x_{N+1}). \quad (1)$$

The anti-symmetrization operator A accounts for exchange between the target electrons and the scattering electron; x_N represents the spatial and spin coordinates of the Nth electron, and φ_i^N represents the wavefunction for the ith N-electron target state. The χ_i^{N+1} are multicentered, square-integrable (L^2) correlation configuration functions where the scattering electron occupies a target molecular orbital. u_{ij} are the continuum orbitals used to represent scattering electrons. The a_{ijk} and b_{ik} are variational parameters, which are determined by solving the secular equation in the inner region.[37] The sum in the first term defines target and continuum configurations, in which the scattering electron is in the continuum and the other electrons in a given state of the target. The second sum term in Eq. (1) represents short-range correlation effects. In the present calculations, Gaussian-type orbitals (GTOs) are used to represent both the bound and the continuum orbitals. The energy-independent inner region wavefunctions Ψ_k^{N+1} are used to construct the R-matrix at the boundary between the inner and outer regions.

In the scattering calculations, the particular choice of the number of target electronic states and the type of L^2 configuration functions included in the expansion (1) defines different scattering models: static exchange (SE), static exchange plus polarization (SEP), and close coupling (CC). In the SE and SEP approximations, only the ground target state wavefunction calculated at the Hartree–Fock (HF) level is considered. SE is the simplest scattering model, in which the L^2 configurations correspond to placing the scattering electron in an unoccupied target orbital of the appropriate symmetry. The SE level only gives an approximation for shape resonances. In the SEP model, the molecule is polarized by promoting one electron from the valence space to a selected number of virtual orbitals (VOs), and the effect is described by adding to the L^2 configurations used in the SE model. The L^2 configurations correspond to single excitations from the ground state configuration of the target molecule and can be written as

$$(\text{core})^{N_c} (\text{valence})^{(N_v - 1)} (\text{virtual})^2, \quad (2)$$

where N_c is the number of electrons in doubly occupied orbitals and N_v is the number of electrons in the valence orbitals, $N_c = 24$ and $N_v = 18$ for pyridine in the present work. The SEP model describes shape resonances very well and can give core-excited resonances. However, the SE and SEP models are only capable of describing elastic collisions. The more sophisticated CC model includes low-lying target states in expansion (1); a complete active space configuration interaction (CASCI) approach is usually used to describe the target states.[38] In our CC model, the L^2 configurations are generated by allowing the scattering electron to occupy one of the orbitals in

the active space or a set of VOs. The $N + 1$ configurations can be represented as

$$(\text{core})^{N_c} (\text{valence})^{N_{as}} (\text{continuum})^1, \quad (3)$$

$$(\text{core})^{N_c} (\text{valence})^{(N_{as}+1)}, \quad (4)$$

$$(\text{core})^{N_c} (\text{valence})^{N_{as}} (\text{virtual})^1, \quad (5)$$

where N_{as} represented as active electrons in the complete active space (CAS), with $N_c = 30$ and $N_{as} = 12$ in the present calculations. Note that including configurations of the form

$$(\text{core})^{N_c} (\text{valence})^{(N_{as}-1)} (\text{virtual})^2 \quad (6)$$

would allow a more complete representation of polarization effects along the line of the SEP approximation, see Eq. (2). However, such configurations can also contribute to an improved treatment of target correlation and therefore lead to an unbalanced model.[38] The CC model includes electronically inelastic channels and is thus capable of describing electronic excitation scattering processes. This makes the CC model especially suitable for the study of Feshbach resonances.

The energy-dependent R-matrix is constructed on the boundary between the inner and outer regions, and then propagated to the asymptotic region to determine the K-matrix by matching to asymptotic functions obtained from Gailitis expansion.[39] Then, T-matrices can be obtained from K-matrices using the relation below,

$$T = \frac{2\,iK}{1 - iK}, \quad (7)$$

which are then used to obtain various scattering cross sections. Eigenphases, obtained from the K-matrix, are used to determine positions and widths of resonances. Here, our calculations were performed using the QEC (Quantemol electron collisions) expert system,[40] which runs both MOLPRO[41] for target models and the UK molecular R-matrix (UKRmol+) code[42] for scattering processes. Differential and momentum transfer cross sections were obtained by using UKRmol+ K-matrices directly in program POLYDCS.[43]

III. COMPUTATIONAL DETAILS

A. Target models

The accuracy of a scattering calculation relies on the use of an appropriate target description. Pyridine has 42 electrons and belongs to C_{2v} symmetry. The orbitals in the pyridine ring are similar to those of benzene, and there are six π-electrons from the three double bonds in the aromatic structure. The equilibrium geometry of pyridine was obtained from the NIST CCCBDB database QCISD/6-311G** level calculation.[25] The Hartree–Fock electronic configuration for ground $X\,^1A_1$ state is described as $1a_1^2\,1b_2^2\,2a_1^2\,3a_1^2\,2b_2^2\,4a_1^2\,5a_1^2\,6a_1^2\,3b_2^2\,7a_1^2\,4b_2^2\,8a_1^2\,5b_2^2\,9a_1^2\,6b_2^2$ $10a_1^2\,1b_1^2\,7b_2^2\,11a_1^2\,2b_1^2\,1a_2^2$.

We separately performed HF and state-averaged complete active space self-consistent field (SA-CASSCF) calculations with a cc-pVTZ basis set to generate the target orbitals for the SEP and CC scattering calculations. Use of augmented diffuse basis functions would lead to the need to use very extended inner regions, which leads to considerable computational complications.[44] Having a model that adequately describes the target excited states is crucial for modeling the computationally tricky Feshbach resonances. In the SA-CASSCF calculations, the choice of active space is crucial to the success of the method because the number of electrons occupying the active orbitals contributes to the accuracy of the description of the wave function. We tested and compared different active spaces in terms of target description accuracy. Finally, we frozen 30 electron in closed orbitals, with the remaining 12 electrons allowed to move freely in the eight active orbitals, CAS(12, 8), to represent our target in the present work. In order to obtain reliable core-excited type of resonance, the inclusion of configurations describing electronically excited states of the target is necessary. Here, a total of 40 target excited states were included in the CC scattering calculations.

Low-energy scattering is dominated by dipole interactions, so an accurate target description is essential when comparing the measurements. Pyridine has a relatively large permanent dipole moments, and our calculated dipole moment of 2.279 D at the HF level and 2.294 D at the SA-CASSCF level are in good agreement with the experimental value of 2.19 D.[25] The vertical ionization threshold of 9.45 eV at HF level is 0.06 eV lower than the experimental data[25] of 9.51 eV. Moreover, the vertical excitation thresholds for the energies up to 8 eV included in the CC expansion are listed in Table I. The calculated results are all higher than the experiments.[45,46] The minimum vertical excitation energy difference is 0.54 eV for the first $1\,^3A_1$ excited state compared to the experiments of Walker *et al.*,[46] and the maximum difference is 1.35 eV for the $1\,^1A_1$ state. The vertical excitation of $1\,^1B_1$ and $1\,^1B_2$ states is both lower than the theoretical values used in the SMC study.[21]

B. Scattering calculations

The scattering calculations were carried out using the SEP and CC approximations. We used both HF and SA-CASSCF orbitals separately generated from the above target descriptions. An R-matrix radius of $a = 13\ a_0$ was selected for the calculations with the

TABLE I. The vertical excitation energies in eV of the first ten target excited states calculated using SA-CASSCF with a cc-pVTZ basis set, along with the theoretical[21] and experimental[45,46] data.

Target state	Present	Theory[21]	Exp1.[45]	Exp2.[46]
$1\,^3A_1$	4.646	3.482	3.86	4.1
$1\,^3B_1$	5.190	⋯	4.12	4.1
$1\,^3B_2$	5.555	4.672	4.47	4.84
$2\,^3A_1$	5.627	5.004	⋯	4.84
$1\,^1B_1$	5.833	6.123	4.78	⋯
$1\,^1B_2$	5.965	6.116	4.99	⋯
$1\,^3A_2$	6.299		5.40	5.40
$1\,^1A_2$	6.381		5.40	5.43
$2\,^3B_2$	6.857		6.09	⋯
$1\,^1A_1$	7.652		6.30	6.30

compact basis set, cc-pVTZ, without augmented diffuse functions; test calculations showed that use of $a = 14\ a_0$ had little effect on the results. The continuum orbitals up to $\ell_{max} = 4$ partial waves are explicitly included. Pyridine has a large permanent dipole, so Born closure procedure[47] is used to compute the effect of the long-range interaction neglected when only partial waves from 0 to 4 are considered. The higher partial waves are included in scattering T-matrices via analytic Born T-matrices. In the scattering calculations, the description of the N-electron target states and the $(N + 1)$-system functions Ψ_k^{N+1} should be balanced. This means that the number of virtual orbitals used for the χ_i in Eq. (1) should be chosen carefully to avoid over correlated wavefunctions. We compared the number of gradual inclusion of VOs to help to identify the resonances and to test the effect on cross sections. Finally, we employed 50 and 60 virtual orbitals in our SEP model, 80 virtual orbitals in our CC model. Resonance positions and widths were automatically detected and fitted using the eigenphase sum to a Breit–Wigner profile using the program RESON.[48]

In Sec. IV, we provide resonance parameters and rotationally summed total elastic cross sections (TECS) using both SEP and CC models for comparison. As POLYDCS can only treat a single electronic state, the rotationally unresolved momentum transfer cross sections (MTCS) and differential cross sections (DCS) are obtained from the SEP model only. The inelastic electronic excitation cross sections (EECS) are calculated on CC model.

IV. RESULTS AND DISCUSSION

A. Resonances

Pseudo-resonances may be present in any calculations at scattering energies above the first states omitted from the calculation. This means that SEP calculations must be treated with caution above the electronic excitation threshold and, while CC calculations extend the energy range, there will always be problems providing reliable information on physical resonances if the scattering energy becomes too high. Table II summarizes all the resonances identified in our calculations using the SEP and CC models with different numbers of virtual orbitals, together with the previous calculations[21] and experiments.[13,14] A resonance appears in the eigenphase sum, see

Fig. 2, as a jump of approximately π radian that reflects the resonance position. We can see that the eigenphase sums show a pronounced structure with many of the features present in the calculations using both models.

Table II shows our resonance positions and widths, and the resonance positions are given up to 8 eV as pseudo resonances may be present at higher energies. A shape resonance is formed by an electron attaching to a molecule in its ground electronic state, usually at incident electron energies below the first target excited threshold energy. Above this energy, resonances usually have a core-excited or mixed shape–core-excited character. As shown in Table II, our first three $1\ ^2B_1$, $1\ ^2A_2$, and $2\ ^2B_1$ resonance positions and widths compare to the previous R-matrix results[22] very well, especially from SEP model with the VOs of 50. The lowest $1\ ^2B_1$ shape resonance with positions of 0.709 eV (VOs = 50) and 0.615 eV (VOs = 60) in the SEP model lies at a lower energy than in the CC calculation but matches the experimental results[13,14] very well. The second $1\ ^2A_2$ resonant state is respectively located at 1.217, 1.102, and 1.076 eV in the SEP(VOs = 50), SEP(VOs = 60), and CC models, which also agrees well with the measurements; this is also a pure shape resonance. Additionally, it can be seen that the second $1\ ^2A_2$ shape resonance at 1.076 eV lies lower than the SEP and other referenced results, indicating that the high-energy shape resonance obtained from the CC model is more sensitive to polarization effects included by increasing the number of virtual orbitals. The third $2\ ^2B_1$ resonance appears higher in energy than the experimental results but below the SMC method results.[21] As this resonance has a mixed shape and core-excited character, similar to the third resonance in pyrazine,[33] its position can be linked to that of the nearby electronically excited states, which are also higher than the observations. Thus, even with up to 80 virtual orbitals included for the target in the CC model, the third resonance remains higher than the measurements:[13,14] the effect of including more VOs was found to make little difference; further improvements would require an enhanced target model allowing for a better treatment of correlation effects in the both the target and anionic wavefunctions.

A core-excited resonance is formed when the incoming electron excites the target molecule to an electronically excited state (parent state) and simultaneously is temporarily trapped in one of

TABLE II. Resonance positions (and widths) in eV for pyridine identified in our R-matrix method with SEP and CC calculations and the number of virtual orbitals (VOs) indicated, compared to previous R-matrix calculations,[22,23] SMC calculations,[21] and the available experimental data.[13–15]

Symmetry	SEP (VOs = 50)	SEP (VOs = 60)	CC (VOs = 80)	R-matrix[23] TIMEDEL	R-matrix[22] RESON	SMC[21]	Exp1[13]	Exp2[14]	Exp3[15]
$1\ ^2B_1$	0.709 (0.026)	0.615 (0.019)	0.829 (0.047)	0.96 (0.07)	0.77 (0.022)	0.90	0.62	0.72	0.79 ± 0.03
$1\ ^2A_2$	1.217 (0.037)	1.102 (0.027)	1.076 (0.038)	1.32 (0.08)	1.11 (0.025)	1.33	1.20	1.18	1.15 ± 0.03
$2\ ^2B_1$	5.470 (0.616)	5.354 (0.591)	5.665 (0.354)	5.08 (0.37)	5.51 (0.48)	5.80	4.58	4.48	4.71 ± 0.02
$1\ ^2A_1$	7.520[a]		6.044 (0.090)	6.30 (0.20)					
$1\ ^2B_2$			6.280[a]	6.76 (0.13)					
$3\ ^2B_1$			6.380[a]	6.21 (0.63)					
$2\ ^2A_2$	7.580 (0.033)	7.521 (0.033)	6.954 (0.222)	6.38 (0.35)					
$4\ ^2B_1$	7.297 (0.052)	7.244 (0.051)	7.263 (0.212)	7.37 (0.47)					7.27 ± 0.08 7.86 ± 0.08

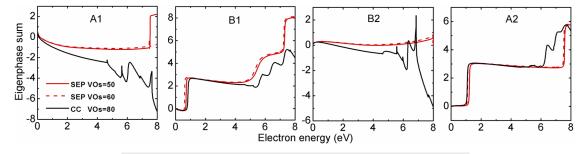[a]Position estimated directly from the eigenphase sums.

FIG. 2. Eigenphase sums for all symmetries for pyridine at SEP and CC approximations.

the unoccupied spin orbitals. These resonances usually happen at higher incident electron energies than shape resonances, since they need enough energy to excite the target. Feshbach resonances are core-excited resonances that lie below their parent target state; they generally have longer lifetimes than core-excited shape resonances. Thus, the $1\ ^2A_1$ resonant state has a narrow resonance width of 0.09 eV from the CC calculation, suggesting it is a Feshbach resonance. The other four resonances ($1\ ^2B_2$, $3\ ^2B_1$, $2\ ^2A_2$, and $4\ ^2B_1$) are located at higher energies in the range of 6–8 eV; they are also core-excited resonant states, but further work is to classify them as mixed or core excited shape resonances. The CC model gives two more resonances ($1\ ^2B_2$ and $3\ ^2B_1$) than the SEP model. As the CC calculations are based on an expansion of 40 excited target states, they are more suitable for representing Feshbach resonances associated with the various excited states. Eigenphases do not vary smoothly across electronic excitation thresholds, and as a result, RESON struggles with resonances that lie close to a threshold. RESON failed to detect the $1\ ^2B_2$ and $3\ ^2B_1$ resonances in our CC calculations; these resonances lie very close to the $1\ ^3A_2$ and $1\ ^1A_2$ excited target states, respectively. The eigenphase sums for B_1 and B_2 symmetries plotted in Fig. 2 do show clear evidence for these additional π resonances. The positions of 7.520 eV for the $1\ ^2A_1$ resonance from the SEP model, as well as 6.280 and 6.380 eV for the $1\ ^2B_2$ and

$3\ ^2B_1$ resonances from the CC model, were estimated directly from the eigenphase sums. Compared to the resonance energies obtained by Sieradzka,[23] who fitted the largest eigenvalues of the time-delay matrix using TIMEDEL code,[49] our minimum and maximum differences from $4\ ^2B_1$ and $2\ ^2B_1$ resonant state energies are 0.10 and 0.58 eV, respectively. In addition, our highest $4\ ^2B_1$ resonance position of 7.263 eV compares well with 7.27 ± 0.08 eV measured from Mathur and Hasted,[15] but a bit higher than the reference value 7.0 eV given by Ryszka et al.[16]

B. Total elastic cross sections and momentum transfer cross sections

In this section, we discuss the total elastic cross sections (TECS) and momentum transfer cross sections (MTCS) below 10 eV. In our experience,[50] increasing the number of VOs from 50 to 60 has little effect on the scattering cross section results, so the following cross sections based on the SEP calculations were selected from 60 VOs for discussion. Our Born-corrected and uncorrected TECS using the SEP and CC models are shown in Fig. 3, compared to the experiments[18,19] as well as the SMC method[21] and the previous R-matrix[22] results. The present uncorrected TECS shows that there are two pronounced peaks below 2 eV, locatedc at around
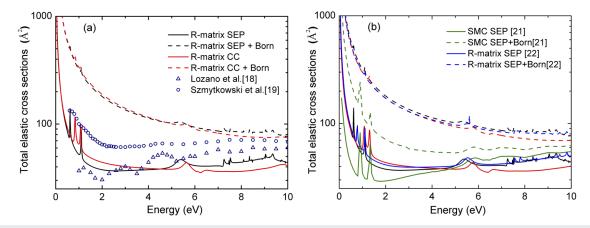

FIG. 3. Total elastic cross sections for electron scattering from pyridine with and without born correction using R-matrix method compared to (a) experimental results from Lozano et al.[18] and Szmytkowski et al.[19] (b) SMC method[21] and R-matrix method[22] calculated results.

0.7 and 1.1 eV, respectively, which are attributed to the formation of two shape-resonant nature ($1\,^2B_1$ and $1\,^2A_2$) in Table II. Another broader structure is located between 5 and 6 eV, that is related to the formation of the third $2\,^2B_1$ mixed character of shape and core-excited resonant state. Moreover, a weak hump from the CC approximation curve is perceptible between 6 and 7 eV, which is associated with the core-excited resonances ($1\,^2A_1$, $1\,^2B_2$, and $3\,^2B_1$) detected above. The pronounced rise in the TECS as the incident energy decreases below 1 eV is due to the strong permanent dipole moment of pyridine. Above 7 eV, our SEP calculations suffer from the presence of pseudo resonances, which appear very narrow spikes in the cross section.

The TECS calculations with the Born approximation from the SEP and CC models nearly overlap over the whole energy region. Whereas both are higher than the measurement results of Lozano *et al.*[18] and Szmytkowski *et al.*[19] for energies up to 7 eV in Fig. 3(a). Lozano *et al.*[18] suggest that this is partly due to the measurements not including rotational excitation, which the calculations do. However, there are also issues with the experimental acceptance angle for strongly forward scattered collisions, which lead to serious difficulties in determining experimental total collision cross sections, as discussed by Zhang *et al.*[51]

As shown in Fig. 3(b), our TECS agree very well with the previous results of the R-matrix method. The R-matrix Born corrected TECS are higher than those obtained from the SMC method[21] at all energies. Conversely, in Fig. 4, the R-matrix MTCS is much smaller than the SMC MTCS[21] but fairly similar in shape. The sudden increases in the MTCS values at around 0.6 and 1.1 eV are due to the $1\,^2B_1$ and $1\,^2A_2$ shape resonances and match the features seen in the TECS. The differences between the R-matrix and SMC calculations might be due to the different electron distribution in L^2 configurations and the different number of partial waves. Our R-matrix calculations all use $\ell_{max} = 4$ over the whole energy range, meaning that fewer partial waves are included than in the SMC calculations[21] above 5 eV. The angular range of integration

could mainly contribute to the cross section differences, especially the results involving the Born corrections. The SMC cross sections are obtained by integrating the corresponding DCS between 1° and 180°, whereas the R-matrix cross sections correspond to the integration over the whole energy range, as mentioned by Sieradzka *et al.*[22]

C. Comparison of differential cross sections

Figure 5 shows a two-dimension DCS distribution for elastic electron collisions with pyridine in the energy range 0–15 eV using the SEP model with 60 VOs. As we can see, the DCS results are largest for scattering angles from 0° to 25°. The elastic DCSs with Born correction as a function of the scattering angle from 0° to 180° for each incident energy (1.1, 2, 3, 3.5, 4, 4.9, 6, 8.5, and 10 eV) are shown in Fig. 6, compared to the previous R-matrix results of Sieradzka *et al.*[22] and SMC results of Barbosa *et al.*,[21] together with the DCS measurements of similar molecular structures from benzene,[27] pyrazine,[32] and pyrimidine.[29] Combining Figs. 5 and 6, we note that the DCS distributions tend to be flat for scattering angles above 40° with increasing incident energy. However, below 40°, the DCSs rapidly increase as the scattering angle tends to zero.

Above 40°, the agreement between our calculated DCSs and the available experimental data from similar the systems of benzene,[27] pyrazine,[32] and pyrimidine[29] are remarkably overlapped at 6 and 10 eV, indicating that the replacement of one or two CH groups in benzene by nitrogen atoms has little effect on the DCS, especially at higher scattering angles and energies. Thus, we conclude that the experimental DCS of a similar pyridine would have the same order of magnitude as these three molecules. Nevertheless, below 40°, the DCS differences between polar pyridine and non-polar benzene and pyrazine increases as the incident energy decreases from 6 eV. Especially at 1.1 eV incident energy and angles below 90°, the DCS due to the polar pyridine molecule is very different from the measurements for non-polar benzene. This is due to the domination of scattering processes by the permanent dipole moment of a polar molecule at low incident energies and scattering angles. At 3 eV, the DCSs from the polar species pyridine with 2.19 D[25] and pyrimidine with 2.334 D[26] are similar, and both are generally higher than non-polar molecular benzene and pyrazine results at low scattering angles. In addition, our DCS calculations nearly overlap the previous R-matrix
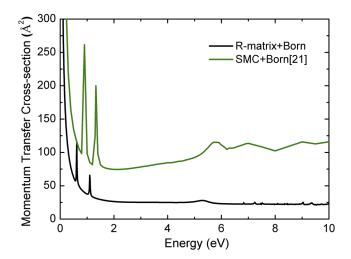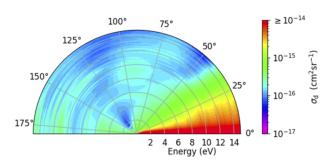

FIG. 4. Momentum transfer cross sections for elastic scattering of electrons by pyridine, the Born closure is employed for the R-matrix with the SEP approximation, compared to the theoretical SMC results.[21]

FIG. 5. The two-dimension differential cross-section distribution for elastic electron collisions with pyridine.
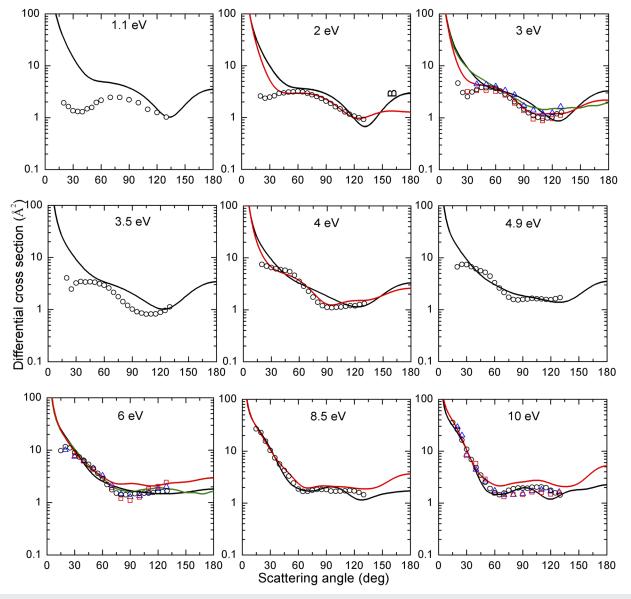
FIG. 6. Elastic differential cross sections for incident energies of 1.1, 2, 3, 3.5, 4, 4.9, 6, 8.5, and 10 eV (black line). Comparison of the theoretical data of the previous R-matrix method[22] (green line), SMC method[21] (red line), as well as the differential measurements of benzene[27] (black circle), pyrazine[32] (red square), and pyrimidine[29] (blue triangle).

results based on the use of a compact basis set[22] at the incident energies of 3 and 6 eV. On the whole, the agreement between R-matrix and SMC results is good, especially at small angles ($\leq 10°$). The R-matrix DCSs perform better than SMC calculations[21] beyond the first electronic excitation threshold (6, 8.5, and 10 eV).

D. Electronic excitation cross sections

Analysis of the inelastic electronic excitation cross sections can provide additional information about resonances lying at energies beyond the first vertical excitation energy. Figure 7 presents EECSs resulting from the electronic transition from ground state X $^1A_1$ to the first eight singlet and triplet excited states, including 1 $^3A_1$, 1 $^3B_1$, 1 $^3B_2$, 2 $^3A_1$, 1 $^1B_1$, 1 $^1B_2$, 1 $^3A_2$, and 1 $^1A_2$ target states. As can be seen, the contribution of the 1 $^3A_1$ triplet states dominates other excitations. This is due to the larger spin multiplicity and lower thresholds of the triplet states compared to their corresponding singlet states. The secondary contribution comes from 1 $^3B_1$, 1 $^3B_2$, and 2 $^3A_1$ triplet excitation states. The inelastic cross sections from the last four 1 $^1B_1$, 1 $^1B_2$, 1 $^3A_2$, and 1 $^1A_2$ excited states are very minor.
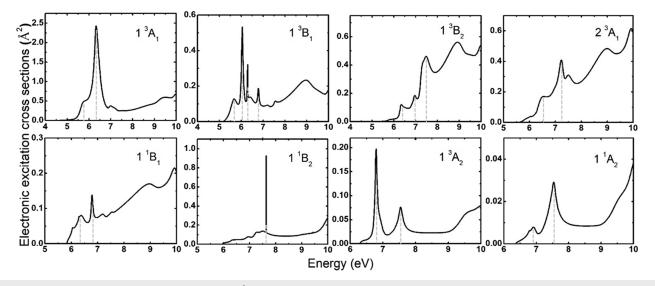
FIG. 7. Electronic excitation cross sections from the ground $X\,^1A_1$ target state to the eight lowest-lying electronic excited states. The vertical dashed lines represent the peak structures, which correspond to the detected resonance positions.

The core-excited resonances in Table II are clearly visible in the corresponding electronic excitation curves in Fig. 7. First, the small structure of the first two $1\,^3A_1$ and $1\,^3B_1$ excited state cross sections was seen between 5 and 6 eV, revealing the mixed-character resonance of the $2\,^2B_1$ symmetry at a position of 5.665 eV. There exist several peaks between 6 and 7 eV except the $1\,^1B_2$ excited state, which was caused by significant contributions of the core-excited resonances of $1\,^2A_1$, $1\,^2B_2$, and $3\,^2B_1$. While no resonances are detected in the SEP calculation in this region in Table II, confirming that the SEP model cannot give an accurate description of the Feshbach resonance. The electronic transitions from the ground $X\,^1A_1$ state to $1\,^3B_2$, $1\,^1B_1$, and $1\,^1A_2$ show a peak at around 7 eV, showing the influence of the $2\,^2A_2$ core-excited resonance. Resonance spike positions between 7 and 8 eV are observed for the EECS of $1\,^3B_2$, $2\,^3A_1$, $1\,^1B_2$, $1\,^3A_2$, and $1\,^1A_2$ electronic states, which is related to the influence of the $4\,^2B_1$ core-excited resonant state. Above 8 eV, there is a broad peak for some EECSs, which seems to be due to a threshold effect associated with the ionization threshold at around 9.50 eV rather than resonances. We suggest that the R-matrix cross sections should be preferred only up to the target ionization threshold as discussed by Sinha and Antony.[52]

V. CONCLUSIONS

We present elastic and inelastic scattering cross sections along with the resonances for low-energy electron collisions with pyridine computed using the R-matrix method within the SEP and CC approximations. The $1\,^2B_1$ and $1\,^2A_2$ low-lying shape resonances and the $2\,^2B_1$ mixed shape agree well with experimental results and prior calculations. Above the first electronic excitation threshold, five higher core-excited resonances ($1\,^2A_1$, $1\,^2B_2$, $3\,^2B_1$, $2\,^2A_2$, and $4\,^2B_1$) are reported, which have not been described by earlier work. The $1\,^2B_1$ and $1\,^2A_2$ shape resonances largely account for

the peak structures in the elastic scattering process, especially in the total elastic cross sections and momentum transfer cross sections. The Born corrected total elastic cross sections are higher than the experiments in the energy up to 10 eV. This is probably due to the acceptance angle of the experiment for strongly forward-scattered collisions.

We analyze the difference in differential cross sections of pyridine from those earlier experimental studies on benzene, pyrazine, and pyrimidine. The agreement between our differential cross section calculations and the previous experimental data of aromatic ring molecule is excellent above 2 eV. Particularly, the substitution of the methine group for nitrogen atoms in going from pyridine to pyrimidine seems to have a small effect on the elastic differential cross-section scattering data above 8 eV. However, below the angle of 40°, the difference in differential cross section becomes obvious between polar pyridine and non-polar benzene as the incident energy decreases from 6 eV, suggesting the importance of the permanent dipole moment for polar azines on differential cross section, especially at low incident energies with narrow scattering angles. The transition between ground $X\,^1A_1$ and $1\,^3A_1$ triplet states mainly contributes to the inelastic electronic excitation cross sections below the ionization threshold. The high core-excited resonances with an effect on the inelastic electronic excitation collision process are found, confirming the success of estimating the core-excited resonances.

AUTHOR DECLARATIONS

Conflict of Interest

The authors have no conflicts to disclose.

Author Contributions

He Su: Conceptualization (equal); Data curation (lead); Formal analysis (lead); Investigation (lead); Methodology (equal); Resources (equal); Software (equal); Writing – original draft (lead); Writing – review & editing (lead). **Xinlu Cheng**: Formal analysis (equal); Investigation (equal); Methodology (equal); Resources (equal); Supervision (equal); Writing – review & editing (equal). **Bridgette Cooper**: Data curation (supporting); Formal analysis (supporting); Investigation (equal); Supervision (supporting). **Jonathan Tennyson**: Formal analysis (equal); Funding acquisition (equal); Methodology (equal); Project administration (equal); Resources (equal); Software (equal); Supervision (equal); Writing – review & editing (equal). **Hong Zhang**: Funding acquisition (equal); Project administration (equal); Resources (equal); Software (equal); Supervision (equal); Writing – review & editing (equal).

DATA AVAILABILITY

The data that support the findings of this study are available from the corresponding authors upon reasonable request.

REFERENCES

[1] I. Baccarelli, I. Bald, F. A. Gianturco, E. Illenberger, and J. Kopyra, Phys. Rep. **508**, 1 (2011).

[2] J. D. Gorfinkiel and S. Ptasinska, J. Phys. B: At., Mol. Opt. Phys. **50**, 182001 (2017).

[3] X. Liu, J. Wu, Y. Yang, T. Wu, and Q. Guo, J. Power Sources **399**, 144 (2018).

[4] A. A. Altaf, A. Shahzad, Z. Gul, N. Rasool, A. Badshah, B. Lal, and E. Khan, "A Review on the Medicinal Importance of Pyridine Derivatives," J. Drug Des. Med. Chem. **1**, 1 (2015).

[5] E. Khan, ChemistrySelect **6**, 3041 (2021).

[6] B. Boudaïffa, P. Cloutier, D. Hunting, M. A. Huels, and L. Sanche, Science **287**, 1658 (2000).

[7] M. A. Huels, B. Boudaïffa, P. Cloutier, D. Hunting, and L. Sanche, J. Am. Chem. Soc. **125**, 4467 (2003).

[8] L. Sanche, Eur. Phys. J. D **35**, 367 (2005).

[9] F. Martin, P. D. Burrow, Z. Cai, P. Cloutier, D. Hunting, and L. Sanche, Phys. Rev. Lett. **93**, 068101 (2004).

[10] R. Barrios, P. Skurski, and J. Simons, J. Phys. Chem. B **106**, 7991 (2002).

[11] H. Hotop, M.-W. Rul, and I. I. Fabrikant, Phys. Scr. **110**, 22 (2004).

[12] S. Ptasińska, S. Denifl, P. Scheier, and T. D. Märk, J. Chem. Phys. **120**, 8505 (2004).

[13] I. Nenner and G. J. Schulz, J. Chem. Phys. **62**, 1747 (1975).

[14] A. Modelli and P. D. Burrow, J. Electron Spectrosc. Relat. Phenom. **32**, 263 (1983).

[15] D. Mathur and J. B. Hasted, Chem. Phys. **16**, 347 (1976).

[16] M. Ryszka, E. Alizadeh, Z. Li, and S. Ptasińska, J. Chem. Phys. **147**, 094303 (2017).

[17] A. T. Dubuis, F. Costa, F. F. da Silva, P. Limão-Vieira, J. C. Oller, F. Blanco, and G. García, Chem. Phys. Lett. **699**, 182 (2018).

[18] A. I. Lozano, J. Jiménez, F. Blanco, and G. García, Phys. Rev. A **98**, 012709 (2018).

[19] C. Szmytkowski, S. Stefanowska, N. Tańska, B. Żywicka, E. Ptasińska-Denga, and P. Możejko, Mol. Phys. **117**, 395 (2019).

[20] N. Gholami, M. Hajivaliei, and M. E. Samei, Appl. Radiat. Isot. **150**, 79 (2019).

[21] A. S. Barbosa, D. F. Pastega, and M. H. F. Bettega, Phys. Rev. A **88**, 022705 (2013).

[22] A. Sieradzka, F. Blanco, M. C. Fuss, Z. Mašín, J. D. Gorfinkiel, and G. García, J. Phys. Chem. A **118**, 6657 (2014).

[23] A. Sieradzka, "Electron attachment to small molecular clusters," Ph.D. thesis, The Open University, 2017.

[24] F. Costa, A. Traoré-Dubuis, L. Álvarez, A. I. Lozano, X. Ren, A. Dorn, P. Limão-Vieira, F. Blanco, J. C. Oller, A. Muñoz, A. García-Abenza, J. D. Gorfinkiel, A. S. Barbosa, M. H. F. Bettega, P. Stokes, R. D. White, D. B. Jones, M. J. Brunger, and G. García, Int. J. Mol. Sci. **21**, 6947 (2020).

[25] NIST Standard Reference Database Number 101, Release 22, edited by R. D. Johnson III (NIST Computational Chemistry Comparison and Benchmark Database, 2022), http://cccbdb.nist.gov/.

[26] G. L. Blackman, R. D. Brown, and F. R. Burden, J. Mol. Spectrosc. **35**, 444 (1970).

[27] H. Cho, R. J. Gulley, K. Sunohara, M. Kitajima, L. J. Uhlmann, H. Tanaka, and S. J. Buckman, J. Phys. B: At., Mol. Opt. Phys. **34**, 1019 (2001).

[28] A. S. Barbosa and M. H. F. Bettega, J. Chem. Phys. **146**, 154302 (2017).

[29] P. Palihawadana, J. Sullivan, M. Brunger, C. Winstead, V. McKoy, G. Garcia, F. Blanco, and S. Buckman, Phys. Rev. A **84**, 062702 (2011).

[30] Z. Mašín, J. D. Gorfinkiel, D. B. Jones, S. M. Bellm, and M. J. Brunger, J. Chem. Phys. **136**, 144310 (2012).

[31] Z. Mašín and J. D. Gorfinkiel, J. Chem. Phys. **137**, 204312 (2012).

[32] P. Palihawadana, J. P. Sullivan, S. J. Buckman, and M. J. Brunger, J. Chem. Phys. **137**, 204307 (2012).

[33] Z. Mašín and J. D. Gorfinkiel, J. Chem. Phys. **135**, 144308 (2011).

[34] C. Winstead and V. McKoy, Phys. Rev. Lett. **98**, 113201 (2007).

[35] J. Tennyson, Phys. Rep. **491**, 29 (2010).

[36] P. G. Burke, R-Matrix Theory of Atomic Collisions: Application to Atomic, Molecular and Optical Processes. (Springer, 2011).

[37] J. Tennyson, J. Phys. B: At., Mol. Opt. Phys. **29**, 1817 (1996).

[38] J. Tennyson, J. Phys. B: At., Mol. Opt. Phys. **29**, 6185 (1996).

[39] M. Gailitis, J. Phys. B: At., Mol. Opt. Phys. **9**, 843 (1976).

[40] B. Cooper, M. Tudorovskaya, S. Mohr, A. O'Hare, M. Hanicinec, A. Dzarasova, J. D. Gorfinkiel, J. Benda, Z. Mašín, A. F. Al-Refaie, P. J. Knowles, and J. Tennyson, Atoms **7**, 97 (2019).

[41] H.-J. Werner, P. J. Knowles, R. Lindh, F. R. Manby, M. Schütz et al., MOLPRO, version 2020.1, a package of ab initio programs 2020, see http://www.molpro.net.

[42] Z. Mašín, J. Benda, J. D. Gorfinkiel, A. G. Harvey, and J. Tennyson, Comput. Phys. Commun. **249**, 107092 (2020).

[43] N. Sanna and F. A. Gianturco, Comput. Phys. Commun. **114**, 142 (1998).

[44] T. Meltzer and J. Tennyson, J. Phys. B: At., Mol. Opt. Phys. **53**, 245203 (2020).

[45] I. Linert and M. Zubek, Eur. Phys. J. D **70**, 74 (2016).

[46] I. C. Walker, M. H. Palmer, and A. Hopkirk, Chem. Phys. **141**, 365 (1989).

[47] N. T. Padial, D. W. Norcross, and L. A. Collins, J. Phys. B: At., Mol. Opt. Phys. **14**, 2901 (1981).

[48] J. Tennyson and C. J. Noble, Comput. Phys. Commun. **33**, 421 (1984).

[49] D. T. Stibbe and J. Tennyson, Comput. Phys. Commun. **114**, 236 (1998).

[50] M. M. Fujimoto, W. J. Brigg, and J. Tennyson, Eur. Phys. J. D **66**, 204 (2012).

[51] R. Zhang, A. Faure, and J. Tennyson, Phys. Scr. **80**, 015301 (2009).

[52] N. Sinha and B. Antony, J. Phys. Chem. A **124**, 3581 (2020).